Microporous and Mesoporous Materials 171 (2013) 139–146

Contents lists available at SciVerse ScienceDirect

Microporous and Mesoporous Materials

journal homepage: www.elsevier.com/locate/micromeso

Layer-by-layer loading iron onto mesoporous silica surfaces: Synthesis, characterization and application for As(V) removal

Feihu Li *

School of Environmental Science and Engineering, Jiangsu Key Laboratory of Atmospheric Environment Monitoring and Pollution Control, Nanjing University of Information Science and Technology, 219 Ningliu Road, Nanjing 210044, China

ARTICLE INFO

Article history:
Received 27 November 2011
Received in revised form 17 December 2012
Accepted 17 December 2012
Available online 27 December 2012

Keywords:
Mesoporous silica
Iron-loaded
Layer-by-layer
Arsenic
Adsorption

ABSTRACT

Iron-bearing minerals have been used as adsorbents for arsenic anions for many decades, but both the small surface area and the poorly defined pore structure limit their performance in removal of arsenic from aqueous systems. Herein, we report a sonochemical layer-by-layer (LBL) loading process for depositing of ferric species onto mesoporous silicas (i.e., MCM-41, SBA-15, and KIT-6). The surface area, pore size and volume, as well as the iron loading of these mesoporous silicas can be tailored and optimized with increasing in loading cycle via a LBL protocol. The surface functioned materials were characterized by X-ray diffraction (XRD), N_2 physisorption, transmission electron microscopy (TEM), Fourier transform infrared (FTIR) spectrometry and zeta potential measurement. Their performance in As(V) adsorption was also tested. The results indicate that the iron-loaded mesoporous silicas retained their ordered pore structure as well as the large surface area, which enable them a good kinetic performance in uptake of As(V) anions. When iron loading is as much as 10 wt.%, two representative iron-loaded silicas Fe_{10}MCM-41 and Fe_{10}KIT-6, exhibited the best performance in trapping the As(V) anions, with an Fe/As molar ratio of about 5.77 and 5.10, respectively. The Fe/As molar ratio implies they belong to the iron-containing adsorbents with the highest adsorption performance for As(V), and therefore could be used as alternative adsorbents for As(V) adsorption.

1. Introduction

Recent report of the crisis caused by arsenic contamination of drinking water in the north part of Jiangsu province, China has attracted wide public attention over the country [1]. To date, such crises of arsenic contamination over the world, especially in Bangladesh and West Bengal, India, Northern China and Western USA were particularly acute and remained a challenge for drinking water supplies [2,3]. On the other hand, the Chinese government has issued a new *Standards for Drinking Water Quality* (*GB 5749-2006*) in which the maximum critical level (MCL) of arsenic was brought down to 0.01 mg L^{-1} [4]. This will be another challenge for the ongoing technologies for arsenic-contaminated drinking water treatment. Hence, it is very urgent to develop effective technologies for the purification of arsenic-contaminated water.

Currently, there are various technologies applicable for the purification of arsenic-contaminated water, such as precipitation/coprecipitation, membrane filtration, adsorption, ion exchange, permeable reactive barriers (PRBs), *etc.* [5] Of these technologies, adsorption has received a special attention and been considered a simple, cost-efficient and byproduct-free approach to remove aqueous contaminants [3,6,7]. In general, the effectiveness of adsorption depends primarily on the adsorbent used. Ferric-based adsorbents such as amorphous ferric oxide [8], poorly crystalline hydrous ferric oxide (ferrihydrite) [9], and goethite (α-FeOOH) [10,11], are well-known for their specific ability to remove both As(V) and As(III) from aqueous solutions. The adsorption capacity of these adsorbents is, however, kinetically limited by the lower interparticle diffusion rate for their lower surface area compared to the iron-loaded adsorbents with high surface area [12]. Many laboratory studies have documented the advantages of iron-loaded adsorbents with high surface area. Gu et al. reported that granular activated carbon-based, iron-containing adsorbents (As-GAC) with ~6% Fe (predominantly in amorphous form) showed the best efficiency in removal of arsenic [13]. They also developed two iron-loaded mesoporous carbon-based sorbents, i.e., the iron-containing mesoporous carbon (IMC) [14] and the iron-modified ordered mesoporous carbon (FeOMC) [15,16], and evaluated their performance in removal of arsenic. Guo et al. found that bead cellulose loaded with iron oxyhydroxide (BCF) with Fe content of 220 mg/mL exhibited adsorption capacities of 99.6 mg As(III)/g BCF and 33.2 mg As(V)/g BCF, respectively at pH 7.0 [17]. Zhang et al. proved that nano-sized hydrated ferric oxide (HFO)-loaded polymeric sorbents with HFO loading of 15% displayed the highest sorption capacity [18]. Chen et al. embedded iron oxide nanoparticles in MCM-41 to obtain

* Tel./fax: +86 25 5873 1090.
E-mail address: fhli@nuist.edu.cn

1387-1811/$ - see front matter © 2012 Elsevier Inc. All rights reserved.
http://dx.doi.org/10.1016/j.micromeso.2012.12.025

a magnetic adsorbent, i.e., Fe^{3+}-magMCM-41, and found that Fe^{3+}-magMCM-41 displayed a selective adsorption of As(V) over Cu(II) [19].

Numerous loading methods to date involved the preparation of iron-loaded mesoporous silicas, including conventional wetness impregnation [20–22], one-pot hydrothermal synthesis [23,24], ion exchange [25,26], solid state loading [27], *etc.* Desirable iron-loaded mesoporous silicas for use as adsorbent would have highly dispersed poorly-crystallized or amorphous iron oxides grafted and/or anchored onto the walls while remaining their high surface area, ordered pore structure and structural stability. However, conventional wetness impregnation especially during drying at elevated temperature may draw the iron precursor out of the channels due to the capillary force, often resulting in blocking of the pore mouths after the annealing process [20–22]. One-pot hydrothermal synthesis could lower the structural ordering of the synthetic materials because of the effect of anions on the condensation of silica precursor, consequently affect the stability of the iron-loaded silica [28]. Solid state loading will yield a highly crystalline iron oxides loaded mesoporous silica [27], which may result in a lower adsorption capacity with respect to arsenic. Sonochemical treatment has been successfully used in the synthesis of mesoporous iron oxide [29]; it will be also effective in iron loading onto the mesoporous silica due to its highly dispersing capacity. Layer-by-layer (LBL) loading is known as a thin film fabrication technique and has been extensively employed to surface functionalization of nanoporous materials [30,31]. Titanium phosphate was loaded onto SBA-15 via a LBL protocol, and displayed a good performance in acid catalysis and metal ion adsorption [30].

In the present study, iron oxides were loaded onto three mesoporous silicas (i.e., KIT-6, MCM-41 and SBA-15) via a solution-based sonochemical LBL loading process for the optimal iron loading for As(V) removal. Data from X-ray diffraction (XRD), N_2 physisorption, transmission electron microscopy (TEM), and Fourier transform infrared spectrometry suggest that the iron oxides were highly-dispersed in the channels and/or mesopores of these silicas as poorly-crystallized hematite nanoparticles. Results from the As(V) adsorption tests indicate that the Iron-loaded mesoporous silicas could effectively adsorb the contaminant anions, and therefore could be used as alternative adsorbents for As(V) removal.

2. Experimental section

2.1. Chemicals

All chemicals except sodium silicate solution (technical grade, approximately 11.3 wt.% Na_2O, 26.7 wt.% SiO_2) were analytical grade and used without any further purification. Pluronic P123 (M_{av} = 5800, $EO_{20}PO_{70}EO_{20}$) and sodium arsenate dibasic heptahydrate ($Na_2HAsO_4{\cdot}7H_2O$) were purchased from Sigma–Aldrich. Cetyltrimethyl ammonium bromide (CTAB), tetraethyl orthosilicate (TEOS), ferric nitrate nonahydrate ($Fe(NO_3)_3{\cdot}9H_2O$, 99%) and other reagents were obtained from Sinopharm Chemical Reagent Co., Ltd.

2.2. Synthesis of iron-loaded mesoporous silica

High-quality MCM-41 was synthesized via a pH adjusting process [32,33]. SBA-15 was fabricated according to the Zhao et al.'s recipe [34]. KIT-6 was prepared following the procedure reported by Ryoo et al. [35].

A solution-based sonochemical LBL procedure was employed to load iron onto the surfaces of these mesoporous silicas (Scheme 1). LBL loading process, specifically reloading a fresh iron oxide layer to the former layer of iron-loaded mesoporous silicas with a lower loading, was used to find optimal iron loading of these mesoporous silicas with respect to As(V) removal. In a typical loading, 9.5 g (~158.3 mmol) of mesoporous silica, e.g., KIT-6, was degassed at 473 K for 2 h and then rapidly impregnated with a 50 mL solution of $Fe(NO_3)_3{\cdot}9H_2O$ (2.6 g (~6.4 mmol), equivalent to 0.5 g of Fe_2O_3) in absolute alcohol (EtOH, 50 mL) with sonochemical treatment (15–20 W, VIRTIS Virsonic-100) and stirring for 0.5 h to ensure fully incorporation of iron precursor to the pores and channels of the host materials. Then, the mixture was evaporated in an open dish at 303 K to a half-dry powder followed by heating up to 673 K at a heating rate of 1 K/min. After cooling to room temperature, the resulting powders, designated as Fe_5KIT-6, was recovered and stored for further use. For an optimal iron loading, the Fe_5KIT-6 was further impregnated with a 6.4 mmol of $Fe(NO_3)_3{\cdot}9H_2O$ in EtOH (50 mL), sonicated, heated to 673 K and cooled to room temperature to achieve Fe_{10}KIT-10. Starting with Fe_{10}KIT-6, Fe_{15}KIT-6 could also be synthesized via the LBL loading procedure. Likewise,

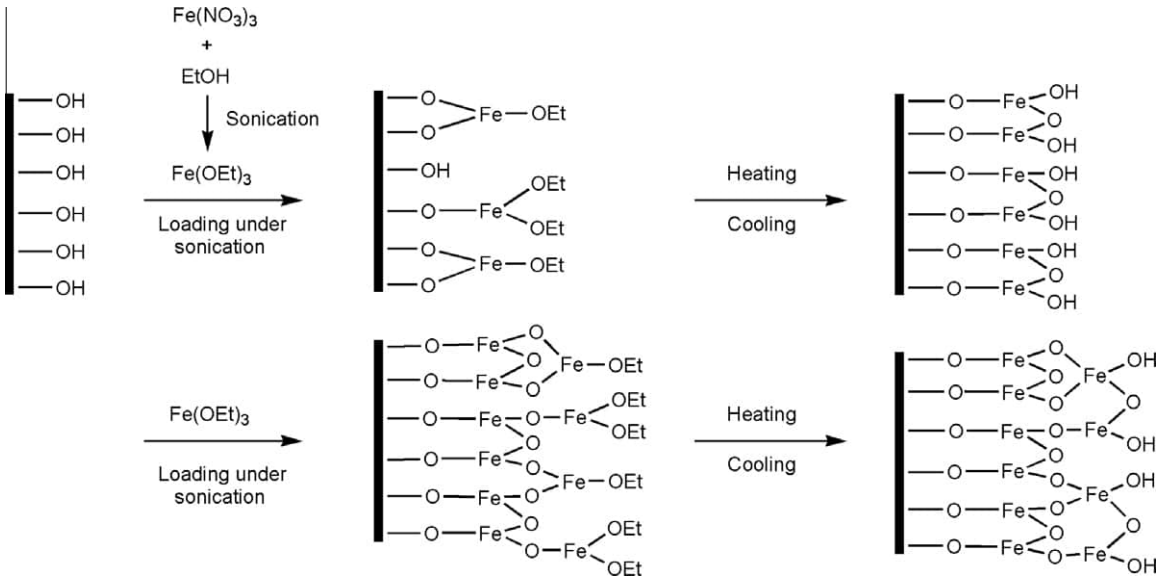

Scheme 1. Surface functionalization of mesoporous silicas by a sonochemical layer-by-layer loading procedure in a $Fe(NO_3)_3$–alcohol system.

Fe_xS (x = 5, 10, and 15; S = MCM-41, SBA-15) could be obtained via the LBL loading protocol mentioned above.

2.3. Characterization

X-ray diffraction (XRD) analysis was conducted using an ARL X'TRA diffractmeter at a voltage of 40 kV and a current of 40 mA with Cu-Kα radiation. Nitrogen physisorption procedure was employed to analyze the surface area, pore volume, and pore size distribution of these materials on a Micromeritics ASAP 2010 apparatus. The Brunauer-Emmett-Teller (BET) method was used to calculate the surface areas, whereas the Barrett-Joyner-Halenda (BJH) algorithm was adopted to evaluate the pore size distribution from the adsorption branch of the isotherm. Transmission electron microscopy (TEM) images and the electron diffraction (ED) patterns were examined on a JEOL JEM-2100 microscope at an accelerating voltage of 200 kV. Fourier transform infrared (FTIR) spectra were recorded on a NIKOLET Nexus870 spectrometer using the pressed KBr pellets of these materials. The zeta potential of typical sorbents was measured at 25 °C using a Zeta Meter (Zetasizer Nano ZS90, Malvern, UK.). The pH of each suspension, consisting of 0.05 g of solid sample in 50 mL of 0.01 M NaCl solution, was adjusted in the range between 2 and 10 using dilute HCl or NaOH, followed by sonication for 30 min before measurement.

2.4. Arsenate adsorption tests

As(V) stock solutions (1000 mg L^{-1}) were prepared using analytical-grade $Na_2HAsO_4{\cdot}7H_2O$ and diluted as needed. Adsorption equilibrium experiments were conducted following the same procedure as described in our previous publication [36]. Adsorption kinetics study were conducted by varying the contacting time (t) of a fixed dose of adsorbent (i.e., 100 mg) with a 100 mL of As(V) solution (10 mg L^{-1}) of a given ionic strength (I, 0.01 M NaCl) at ambient temperature (T, 298 ± 1 K). Typically, to a set of 100 mL of As(V) solution in 250 mL conical flask were added 100 mg of adsorbent and sealed, then the flasks were fixed on a reciprocal shaker and shaken at 180 rpm and 298 ± 1 K for different contacting time, t (i.e., 5, 10, 20, 40, 80, 120, 180, 300, 480 min, respectively). Then the mixtures were filtered with a 45 μm membrane filter for the measurement of As(V) concentration (C_t). The adsorption quantity (q_t) at time t was calculated from $q_t = (C_0 - C_t) \times V/M$, where C_0 is the initial As(V) concentration (=10 mg L^{-1}), V is the volume of the mixture (≈100 mL), and M is the dose of adsorbent added (=100 mg). The kinetic data were fitted with the pseudo second-order kinetic model [37] for depicting the adsorption of As(V) to the selected adsorbents:

$$\frac{t}{q_t} = \frac{1}{v_0} + \frac{1}{q_e}t \quad (1)$$

$$v_0 = k_2 q_e^2 \quad (2)$$

where v_0 (mg g^{-1} min^{-1}) in Eq. (1) is the initial adsorption rate, q_e (mg g^{-1}) is the adsorption capacity at equilibrium, q_t (mg g^{-1}) is the adsorption quantity at time t, and t is contacting time (min), k_2 (g mg^{-1} min^{-1}) in Eq. (2) is the pseudo-second-order rate constant.

Arsenate analysis was performed on an AF-610 atomic fluorescence spectrometer (AFS, Beijing Raleigh Analytical Instrument Co., China) following the hydride-generation atomic fluorescence spectrometry (HG-AFS) procedure [38].

3. Results and discussion

3.1. XRD

As shown in Fig. 1, XRD pattern of KIT-6 shows four well-resolved Bragg peaks assignable to (211), (220), (420), and (422) reflections in the cubic *Ia3d* space group [35]. Upon iron loading, the four peaks were still detected, although not so well resolved as the host KIT-6, implying that the ordered cubic arrangement of uniform mesopores is preserved after the introduction of Fe. The XRD peak intensity shows a gradual decline with increasing iron loading of KIT-6 (*c.f.* traces KIT-6, Fe_5KIT-6, Fe_{10}KIT-6 and Fe_{15}-KIT-6 in Fig. 1a), this is due to the partial occupation of mesopores by the introduced iron oxides [39]. Both Iron-loaded MCM-41 and SBA-15 show a similar decrease in XRD peak intensity as well (see Fig. S1 in the Supporting Information). The wide-angle XRD patterns (Fig. 1b) of iron-loaded KIT-6 were featured with four broad peaks. The peak at $2\theta = 22°$ was owing to amorphous silica [40], while the other peaks at $2\theta = 35.8°$, 39.9°, and 62.0° were attributable to (110), (113), and (214) reflections of a poorly crystallized hematite (JCPDS PDF #24-0072) [41]. The peak intensity of poorly crystallized hematite increases with the increase in iron loading,

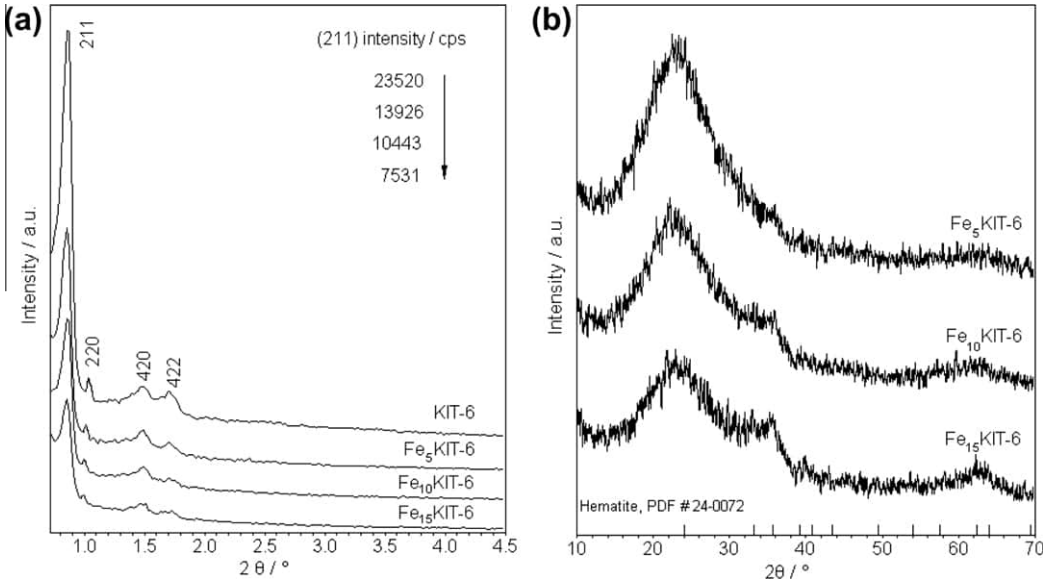

Fig. 1. (a) Small-angle and (b) wide-angle XRD patterns of iron-loaded KIT-6 as a function of the iron loading.

while the peak intensity of amorphous silica decreases as expected (Fig. 1b). However, XRD patterns of iron-loaded mesoporous silica reported in previous literature [22,42] illuminate that the iron oxide precursor, upon annealing, definitely convert to crystalline hematite with well-resolved peaks, conclusively confirming that the LBL loading procedure employed in our work preferredly yield poorly crystallized hematite highly dispersed in the mesopores of host silicas (e.g., KIT-6, SBA-15 and MCM-41).

3.2. N_2 physisorption

Fig. 2 presents the N_2 physisorption isotherms and BJH pore-size distributions of iron-loaded KIT-6 as a function of the iron loading. All species possess a type-IV isotherm with an H1 type hysteresis loop in the relative pressure (p/p_0) range of 0.4–0.8. The hysteresis loops are broadened upon iron oxides loading onto KIT-6 and moreover, the desorption curves slope down with increasing iron loading, implying the presence of partially pore blockage by the iron oxides [43,44]. The specific surface area ($\boldsymbol{S}_{BET}$) of iron-loaded KIT-6 sample decreases from 716 to 572, 545 and 509 $m^2 g^{-1}$ as the iron loading increase from 0 to 5, 10 and 15 wt.%, respectively (Table 1). Besides the decreasing BET surface areas, both the mesopore volumes (V_{meso}) and micropore volumes (V_{micro}) decrease with increasing iron loading as expected. This tendency is also true for both iron-loaded MCM-41 and SBA-15 (see Fig. S2 and Table S1 in the Supporting Information). However, the average pore size (D_{BJH}) of KIT-6 increases from 71.1 to 71.8 Å when loading 5 wt.% iron oxides onto pure KIT-6, and then tends to decrease with increasing iron loading. The phenomenon could be explained as that the silane oligomers in the walls of KIT-6 recondense and shrink upon the sonication-generated heat treatment in the presence of alcohol during the loading procedure, which was also observed in synthesis of highly stable SBA-15 in alcohol system [45]. As the iron loading increase, the average pore sizes (D_{BJH}) of both MCM-41 and SBA-15 are, however, expectedly decreasing without a prior increase upon the sonochemical treatment (see Fig. S2 and Table S1). This is probably due to the difference in the starting silica precursors, i.e., TEOS for KIT-6 while sodium silicate solution for the MCM-41 and SBA-15.

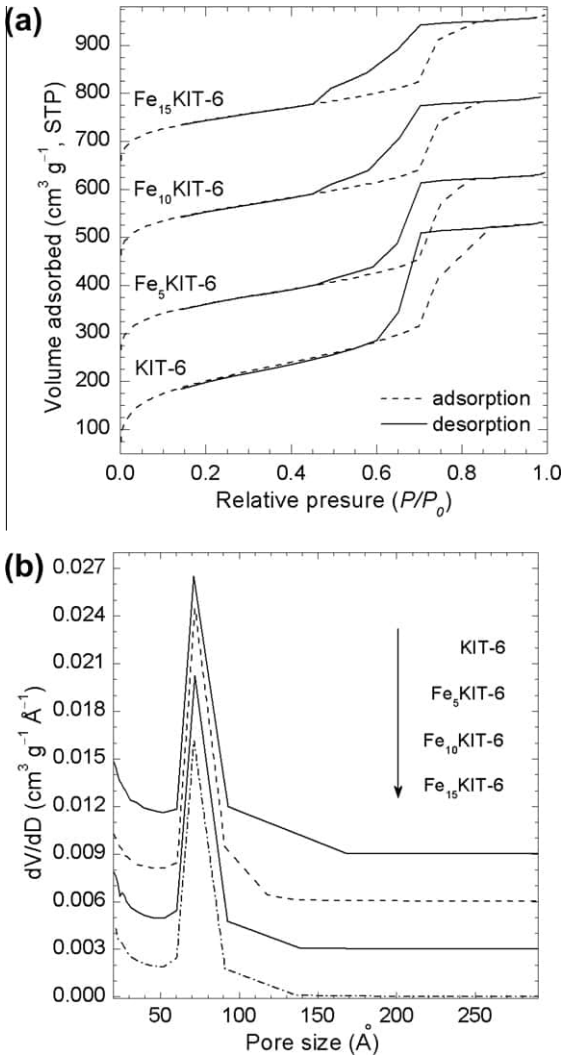

Fig. 2. (a) N_2 physisorption isotherms and (b) BJH pore size distributions of iron-loaded KIT-6 as a function of the iron loading.

Table 1
Textural parameters of KIT-6 as a function of iron loading.

Sample	d_{211} (Å)	a_0 (Å)	$\boldsymbol{S}_{BET}$ ($m^2 g^{-1}$)	V_{meso} ($cm^3 g^{-1}$)	V_{micro} ($cm^3 g^{-1}$)	D_{BJH} (Å)
KIT-6	102.0	249.8	716	0.83	0.06	71.1
Fe_5KIT-6	102.8	251.8	572	0.68	0.06	71.8
Fe_{10}KIT-6	102.6	251.3	545	0.61	0.05	71.6
Fe_{15}KIT-6	102.8	251.8	509	0.56	0.05	71.2

By a simple equation, $H \approx a_0 - D_{BJH}$, where H refers to the wall thickness and a_0 refers to cell parameter of 2D hexagonal *p6mm* mesoporous silicas (e.g. MCM-41, SBA-15), the average thickness of coating layer could be estimated to be 0.5 and 0.2 Å for MCM-41 and SBA-15, respectively (*cf.* Table S1).

3.3. TEM

Iron-loaded KIT-6 species with iron loading of 10 wt.% has been chosen as representative sample for morphological characterization of its mesopores by TEM (Fig. 3). TEM images of Fe_{10}KIT-6 reveal a regular and extended pore periodicity along with highly-dispersed poorly crystallized hematite nanoparticles over the walls and channels (*cf.* Figs. 3a–c). Energy-dispersive X-ray spectroscopy (Fig. 3d) suggests that iron oxides were successfully loaded onto KIT-6. The absence of large crystalline iron oxides grains implies that sonochemical treatment seems to preferredly favor the formation of poorly crystallized hematite in the confined channels. Using MCM-41 and SBA-15 as host materials, the Fe-loaded MCM-41 and SBA-15 also exhibit regular pore structure with highly-dispersed poorly crystallized hematite (see Fig. S3 in the supporting information). The corresponding selected area electron diffractograms (SAED, insets in Figs. S3 b and d) with an amorphous diffuse diffraction ring further verify the poor crystallinity of the loaded hematite.

3.4. FT-IR

The Fourier-transform (FT)-IR spectra of iron-loaded KIT-6 as a function of the iron loading (Fig. 4) exhibits absorption bands at 1078 and 807 cm^{-1}, which are due to antisymmetric stretching mode and symmetric stretching mode of Si–O–Si, respectively. The minor shoulder at 960 cm^{-1} is commonly attributed to the stretching mode of non-bridging oxygen atoms, Si–OH [46]. The broad absorption centered at 3648, and ~3320 cm^{-1} can be ascribed to O–H stretching vibrations due to surface and interlayer H_2O, respectively. The bands at 570 and 460 cm^{-1} are due to a Fe–O vibrational mode in typical poorly crystallized hematite [47]. The minor band at 1632 cm^{-1} may be assignable to the bending vibrations of physically adsorbed water. As to host materials MCM-41 and SBA-15, similar FT-IR spectra to those of Fe_xKIT-6

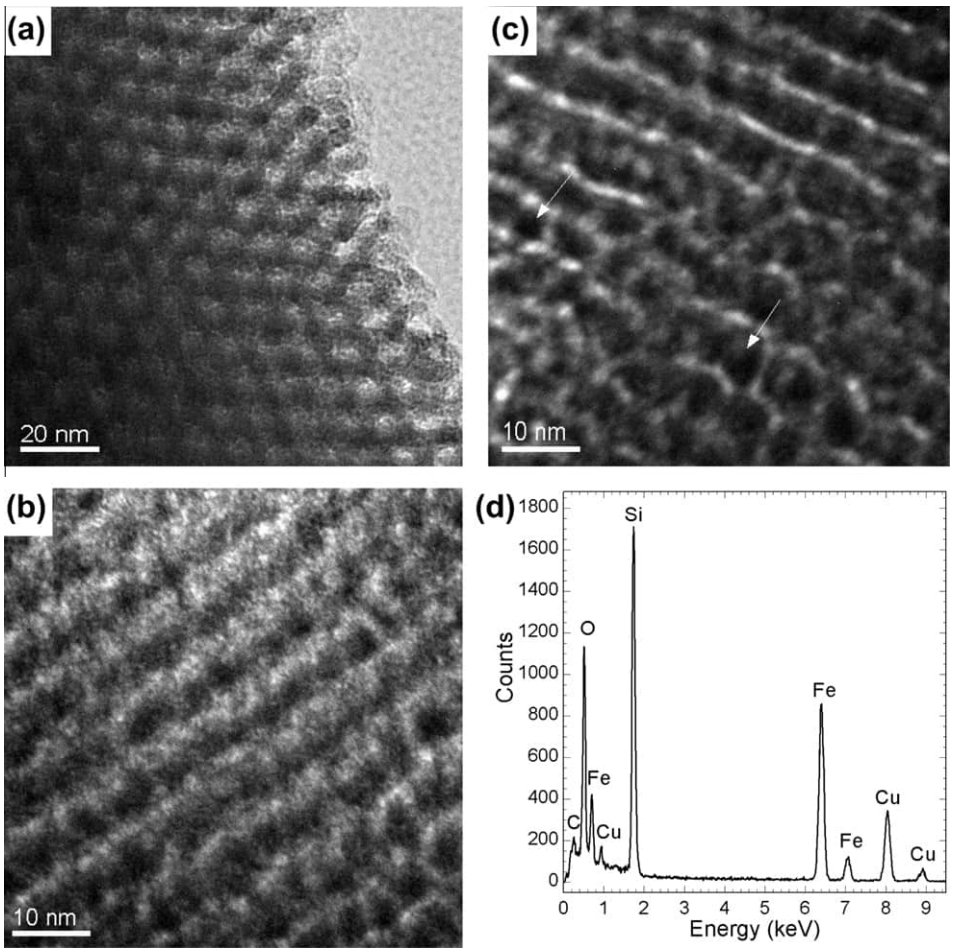

Fig. 3. TEM images (a–c, along [311], [531], and [110] direction) and EDX spectrum (d) of iron-loaded KIT-6 at loading of 10 wt.% (i.e., Fe_{10}KIT-6).

(x = 0, 5, 10, 15) were obtained showing all representative adsorption bands of these IR-active group as afore mentioned (see Fig. S4).

3.5. Zeta potential

The zeta potential profiles of iron-loaded KIT-6 as a function of pH are shown in Fig. 5. The surface of all the iron-loaded KIT-6 samples is positively charged at pH 2.0. With pH value increase from 2.0 to 11.0, KIT-6 firstly becomes negatively charged, followed by Fe_{15}KIT-6, and then Fe_{10}KIT-6, finally Fe_5KIT-6. This behavior of the iron-loaded KIT-6 is mainly attributed to the presence of –O–Fe group (as evidenced by FT-IR, Fig. 4), which are being protonated at low/moderate pH values. The point of zero charge (pH_{PZC}) values of KIT-6, Fe_5KIT-6, Fe_{10}KIT-6, Fe_{15}KIT-6 are 2.3, 3.3, 4.4, 5.2 respectively. The pH_{PZC} of KIT-6 in our study is in reasonable agreement with the isoelectric point (IEP) of KIT-6 (pH_{PZC} = 2.7 ± 0.2) [48] and other mesoporous silica, i.e., SBA-15 (pH_{PZC} = 2.3 ± 0.1) [49]. The pH_{PZC} of iron-loaded KIT-6 increases with increasing iron loading, reflecting that the surface-loaded $FeOH_2^+$ group results in the increased IEP of KIT-6 [50]. The increase of pH leads to increase of FeO^- and decrease of $FeOH_2^+$ group concentrations, consequently affect the adsorption performance of arsenic via electrostatic interactions. The fact that all iron-loaded KIT-6 show a lower pH_{PZC} than pure iron oxide in 0.01 NaCl solution (pH_{PZC} = 7.0) [50], suggests that there is some free surface silanols on the surfaces of the host mesoporous silica KIT-6. The residual surface silanol groups will influence the adsorption process of arsenic.

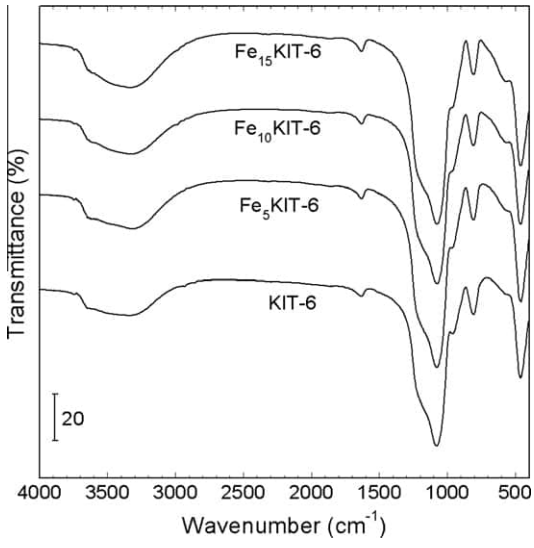

Fig. 4. FT-IR spectra of iron-loaded KIT-6 as a function of the iron loading.

3.6. Adsorption tests for As(V)

3.6.1. Adsorption isotherms

The adsorption results of As(V) onto the selected adsorbents are depicted in Fig. 6, and the fitting data of both Langmuir and

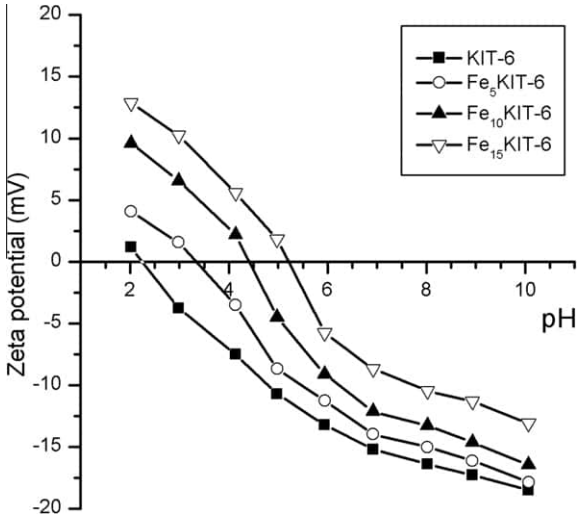

Fig. 5. Zeta potential profiles of iron-loaded KIT-6 versus pH in 0.01 M NaCl solution.

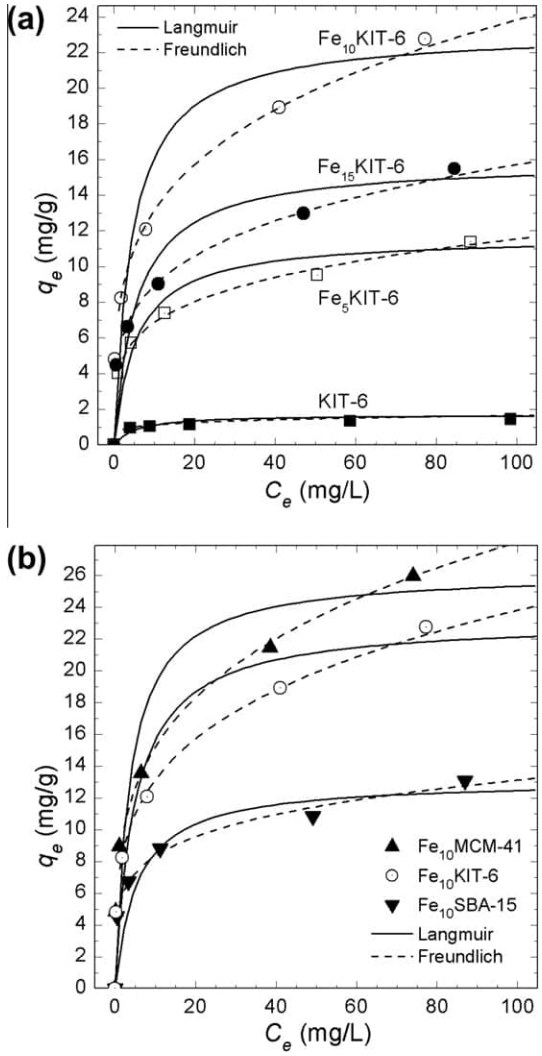

Fig. 6. Adsorption isotherms of (a) KIT-6, Fe_xKIT-6 (x = 5, 10, 15); (b) Fe_{10}S (S = MCM-41, SBA-15, KIT-6), (I = 0.01 M NaCl, pH = 7.0 ± 0.1, T = 298 ± 1 K, t = 24 h).

Table 2
Fitting data of both the Langmuir and the Freundlich equations [Eqs. (3), (4)] for adsorption of As(V) by selected iron-loaded mesoporous silica as a function of the iron loading (298 ± 1 K).

Sorbent	Langmuir			Freundlich		
	b (L mg^{-1})	q_m (mg g^{-1})	R^2	K	n	R^2
KIT-6	0.13	1.07	0.992	0.75	0.16	0.994
Fe_5KIT-6	0.20	11.68	0.981	4.07	1.33	0.996
Fe_{10}KIT-6	0.23	23.20	0.976	7.24	1.69	0.998
Fe_{15}KIT-6	0.18	15.89	0.971	5.06	1.48	0.995
Fe_{10}MCM-41	0.28	26.25	0.952	8.26	1.76	0.997
Fe_{10}SBA-15	0.24	13.12	0.978	5.13	1.39	0.993

Freundlich equations are summarized in Table 2. Both the Langmuir [Eq. (3)] and Freundlich equations [Eq. (4)] were adopted to fit the data:

$$q_e = \frac{q_m \cdot C_e}{b + C_e} \quad (3)$$

$$q_e = KC_e^{1/n} \quad (4)$$

Where q_e (mg As g^{-1} adsorbent) was the amount of arsenic adsorbed and C_e was the equilibrium concentration of arsenic (mg L^{-1}) in the solution. q_m and b were fitting parameters representing the maximum adsorption of arsenic and the adsorption constant, respectively, in the Langmuir model, while K and n were fitting parameters in Freundlich model. The adsorbed amount of arsenic per gram adsorbent (q_e, mg As g^{-1} adsorbent) increased with increasing equilibrium concentration of aqueous arsenic (C_e, mg L^{-1}) as expected. The adsorption data could be fitted reasonably well by both the Langmuir and the Freundlich models, with slightly higher correlation coefficients (R^2) for the Freundlich equation (Table 2), which is in agreement with that of aluminum-incorporated SBA-15 for As(V) adsorption [51]. The calculated maximum adsorption capacity (q_m) of iron-loaded KIT-6 adsorbents increased in the order of Fe_{10}KIT-6 > Fe_{15}KIT-6 > Fe_5KIT-6 > KIT-6 (Table 2 and Fig. 6a), suggesting that Fe_{10}KIT-6 showed the best performance in adsorption of As(V) among three iron-loaded KIT-6 adsorbents. Three primary factors, i.e., the surface area of the adsorbent, the amount of iron loaded, and the affinity of arsenic to iron conclusively determine the performance of iron-containing adsorbents. The best performance of iron-loaded adsorbent in arsenic adsorption achieved once the match of the three factors obtained the best balance. For example, the specific surface areas (S_{BET}) of Fe_5KIT-6 is greater than either Fe_{10}KIT-6 or Fe_{15}KIT-6, whereas the adsorption performance of Fe_{10}KIT-6 is best among the three adsorbents, implying that 10 wt.% of iron loading onto KIT-6 is the optimal dosage, at which the best balance between the surface area of the adsorbent and the amount of iron loaded achieved. When setting the iron loading to 10 wt.%, the adsorption performance will be in positively correlation with the surface area of the adsorbent. For instance, Fe_{10}MCM-41 with the largest surface area showed the best adsorption performance as expected (Tables 1 and 2, Table S1, and Fig. 6b). The molar ratio of iron to arsenic of Fe_{10}MCM-41 and Fe_{10}KIT-6 are about 5.77 and 5.10, respectively, which are among the highest for the iron-containing adsorbents [13,14,16].

3.6.2. Adsorption kinetics

With an initial concentration (C_0) of 10 mg L^{-1}, As(V) adsorption was considerably faster and approximately archived to equilibrium within 2 h for all iron-loaded KIT-6 adsorbents (Fig. 7a). Similar fast adsorption kinetic was also reported in As(V) adsorption onto aluminum-incorporated SBA-15 [51] and iron-containing OMC [16]. The kinetic data have been simulated with the pseudo-second-order rate

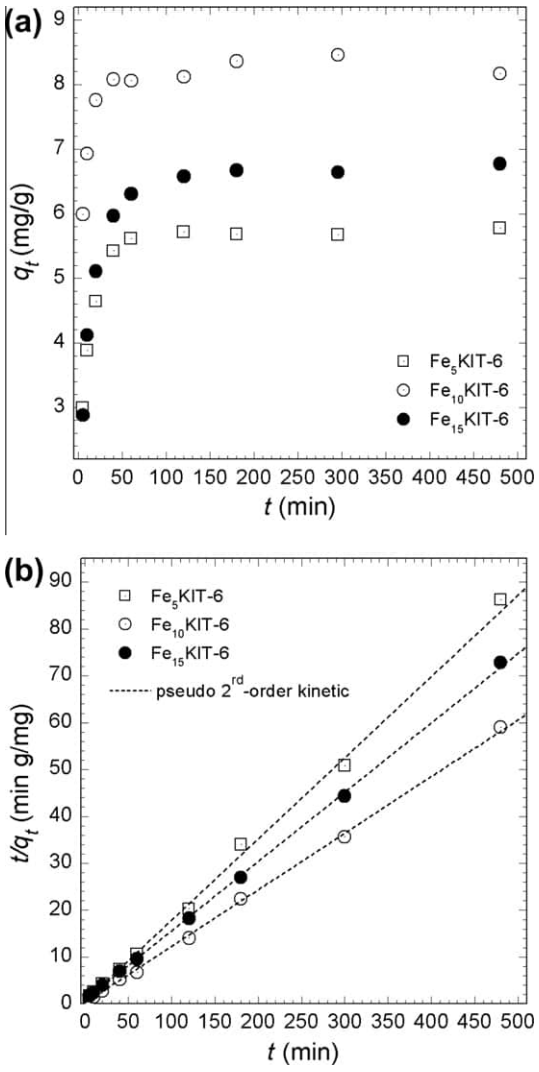

Fig. 7. Kinetic curves of As(V) adsorption onto Fe_xKIT-6 (x = 5, 10, 15): (a) $q_t \sim t$; (b) $t/q_t \sim t$, (I = 0.01 M NaCl; C_0 = 10 mg L^{-1}; pH = 7.0 ± 0.1; T = 298 ± 1 K).

Table 3
Fitting data of the Pseudo second-order rate kinetic equations [Eqs. (1), (2)] for adsorption of As(V) by iron-loaded mesoporous KIT-6 as a function of the iron loading (298 ± 1 K).

Sorbent	Pseudo second-order rate kinetic				
	k_2 (g mg^{-1} min^{-1})	v_0 (mg g^{-1} min^{-1})	q_e (mg g^{-1})	$q_{e.c}$ (mg g^{-1})	R^2
Fe_5KIT-6	0.145	1.80	5.72	5.77	0.997
Fe_{10}KIT-6	0.456	4.68	8.24	8.29	0.993
Fe_{15}KIT-6	0.102	1.18	6.62	6.70	0.991

kinetic model [Eqs. (1), (2)]. Fig. 7b shows the plot of t versus t/q_t to determine the v_0 and $q_{e.c}$>. values for these adsorbents. Table 3 summarizes the determination coefficients (R^2) and several parameters of the pseudo- second-order rate kinetic model. The pseudo-second-order rate model fits closely with kinetic data of all these iron-loaded KIT-6 adsorbents, giving the determination coefficients (R^2) greater than 0.99. The kinetic results also show that the adsorption capacity of iron-loaded KIT-6 samples decreases in the order of Fe_{10}KIT-6 > Fe_{15}KIT-6 > Fe_5KIT-6, which is consistent with previous adsorption isotherm tests.

4. Conclusions

In current work, we demonstrated that the sonochemical LBL loading procedure is capable to deposit ferric species onto mesoporous silicas (i.e., MCM-41, SBA-15 and KIT-6) to obtain iron-loaded mesoporous silicas with highly-dispersed iron oxides. By varying the LBL loading cycles, we can optimize the iron loading with respect to their adsorption performance for As(V) in solutions. Results of XRD, TEM, FTIR, N_2 physisorption in combination with As(V) adsorption tests suggested that the iron-loaded mesoporous materials retain a comparable ordered pore structure and high specific surface area as the host materials, and especially showed an excellent adsorption performance for As(V) when the iron loading was as much as 10 wt.%. Therefore, these iron-loaded mesoporous materials could be potentially used as efficient adsorbents for As(V) removal from aqueous systems.

Acknowledgments

The work was financially supported in part by NSFC (Grant Nos. 51002080, 51076068), the Research Funds of NUIST (Grant No. 20080266) and the Priority Academic Program Development of Jiangsu Higher Education Institutions. The authors are grateful to Prof. Mindong Chen, Prof. Jianping Zhai, Dr. Fengling Liu and Dr. Xiaoru Fu for helpful discussion, to the three referees for their valuable comments.

Appendix A. Supplementary data

Supplementary data associated with this article can be found, in the online version, at http://dx.doi.org/10.1016/j.micromeso.2012.12.025.

References

[1] Jiangsu Pizhou suffers Arsenic contaminations from Shandong Industries. <http://www.chinaenvironment.com/view/ViewNews.aspx?k=20090806180023953>.
[2] P.L. Smedley, D.G. Kinniburgh, Appl. Geochem. 17 (2002) 517–568.
[3] D. Mohan, C.U. Pittman, J. Hazard. Mater. 142 (2007) 1–53.
[4] Chinese Ministry of Public Health and National Standardization Commission, Standards for Drinking Water Quality (GB 5749–2006), 2006.
[5] US EPA, Arsenic Treatment Technologies for Soil, Waste, and Water, EPA-542-R-02-004, Washington, DC, 2002.
[6] H. Genc-Fuhrman, J.C. Tjell, D. McConchie, Environ. Sci. Technol. 38 (2004) 2428–2434.
[7] Y. Zhang, M. Yang, X.M. Dou, H. He, D.S. Wang, Environ. Sci. Technol. 39 (2005) 7246–7253.
[8] T.H. Hsia, S.L. Lo, C.F. Lin, Chemosphere 25 (1992) 1825–1837.
[9] K.P. Raven, A. Jain, R.H. Loeppert, Environ. Sci. Technol. 32 (1998) 344–349.
[10] X.H. Sun, H.E. Doner, Soil Sci. 161 (1996) 865–872.
[11] K.A. Matis, A.I. Zouboulis, F.B. Malamas, M.D.R. Afonso, M.J. Hudson, Environ. Pollut. 97 (1997) 239–245.
[12] D. Mishra, J. Farrell, Environ. Sci. Technol. 39 (2005) 9689–9694.
[13] Z.M. Gu, J. Fang, B.L. Deng, Environ. Sci. Technol. 39 (2005) 3833–3843.
[14] Z.M. Gu, B.L. Deng, Environ. Eng. Sci. 24 (2007) 113–121.
[15] Z.M. Gu, B.L. Deng, Appl. Organomet. Chem. 21 (2007) 750–757.
[16] Z.M. Gu, B.L. Deng, J. Yang, Microporous Mesoporous Mater. 102 (2007) 265–273.
[17] X.J. Guo, F.H. Chen, Environ. Sci. Technol. 39 (2005) 6808–6818.
[18] Q.J. Zhang, B.C. Pan, W.M. Zhang, B.J. Pan, Q.X. Zhang, H.Q. Ren, Ind. Eng. Chem. Res. 47 (2008) 3957–3962.
[19] X.Q. Chen, K.F. Lam, Q.J. Zhang, B.C. Pan, M. Arruebo, K.L. Yeung, J. Phys. Chem. C 113 (2009) 9804–9813.
[20] S.E. Dapurkar, S.K. Badamali, P. Selvam, Catal. Today 68 (2001) 63–68.
[21] R. Kohn, M. Froba, Catal. Today 68 (2001) 227–236.
[22] F. Jiao, B. Yue, K.K. Zhu, D.Y. Zhao, H.Y. He, Chem. Lett. 32 (2003) 770–771.
[23] B. Echchahed, A. Moen, D. Nicholson, L. Bonneviot, Chem. Mater. 9 (1997) 1716–1719.
[24] S. Samanta, S. Giri, P.U. Sastry, N.K. Mal, A. Manna, A. Bhaumik, Ind. Eng. Chem. Res. 42 (2003) 3012–3018.
[25] A.B. Bourlinos, M.A. Karakassides, D. Petridis, J. Phys. Chem. B 104 (2000) 4375–4380.

[26] H.Q. Guo, W. Xu, M.H. Cui, N.L. Yang, D.L. Akins, Microwave absorption by nanostructural ferric oxide encapsulated within MCM-41, Chem. Commun. (2003) 1432–1433.
[27] F. Schuth, A. Wingen, J. Sauer, Microporous Mesoporous Mater. 44–45 (2001) 465–476.
[28] S.N. Che, S.Y. Lin, M. Kaneda, et al., J. Am. Chem. Soc. 124 (2002) 13962.
[29] D.N. Srivastava, N. Perkas, A. Gedanken, I. Felner, J. Phys. Chem. B 106 (2002) 1878–1883.
[30] J. Zhang, Z. Ma, J. Jiao, H. Yin, W. Yan, E.W. Hagaman, J. Yu, S. Dai, Langmuir 25 (2009) 12541–12549.
[31] D.M. Dotzauer, J. Dai, L. Sun, M.L. Bruening, Nano Lett. 6 (2006) 2268–2272.
[32] R. Ryoo, J.M. Kim, J. Chem. Soc. Chem. Commun. (1995) 711–712.
[33] T.R. Pauly, V. Petkov, Y. Liu, S.J.L. Billinge, T.J. Pinnavaia, J. Am. Chem. Soc. 124 (2002) 97–103.
[34] D.Y. Zhao, J.L. Feng, Q.S. Huo, N. Melosh, G.H. Fredrickson, B.F. Chmelka, G.D. Stucky, Science 279 (1998) 548–552.
[35] F. Kleitz, S.H. Choi, R. Ryoo, Chem. Commun. (2003) 2136–2137.
[36] F.H. Li, H. Fu, J.P. Zhai, Q. Li, Microporous Mesoporous Mater. 123 (2009) 177–184.
[37] Y.S. Ho, G. McKay, Chem. Eng. J. 70 (1998) 115–124.
[38] J.B. Shi, Z.Y. Tang, Z.X. Jin, Q. Chi, B. He, G.B. Jiang, Anal. Chim. Acta 477 (2003) 139–147.
[39] W. Liu, S.Y. Lai, H.X. Dai, S.J. Wang, H.Z. Sun, C.T. Au, Catal. Lett. 113 (2007) 147–154.
[40] Y.F. Shi, Y. Meng, D.H. Chen, S.J. Cheng, P. Chen, T.F. Yang, Y. Wan, D.Y. Zhao, Adv. Funct. Mater. 16 (2006) 561–567.
[41] F.H. Li, X.R. Fu, J. Huang, J.P. Zhai, Chem. Res. Chin. Univ. 28 (2012) 559–562.
[42] H.Q. Guo, X.M. Zhang, M.H. Cui, R. Sharma, N.L. Yang, D.L. Akins, Mater. Res. Bull. 40 (2005) 1713–1725.
[43] J. Zhang, Z. Ma, J. Jiao, H. Yin, W. Yan, E.W. Hagaman, J. Yu, S. Dai, Microporous Mesoporous Mater. 129 (2010) 200–209.
[44] M. Kruk, M. Jaroniec, Chem. Mater. 13 (2001) 3169–3183.
[45] J.H. Sun, J.A. Moulijn, J.C. Jansen, T. Maschmeyer, M.O. Coppens, Adv. Mater. 13 (2001) 327–331.
[46] N. Primeau, C. Vautey, M. Langlet, Thin Solid Films 310 (1997) 47–56.
[47] K. Woo, H.J. Lee, J.P. Ahn, Y.S. Park, Adv. Mater. 15 (2003) 1761–1764.
[48] M. Falahati, A.A. Saboury, L. Ma'mani, A. Shafiee, H.A. Rafieepour, Int. J. Biol. Macromol. 50 (2012) 1048–1054.
[49] M. Kokunešoski, J. Gulicovski, B. Matović, M. Logar, S.K. Milonjić, B. Babić, Mater. Chem. Phys. 124 (2010) 1248–1252.
[50] S. Chibowski, M. Wisniewska, Colloids Surf. A 208 (2002) 131–145.
[51] M. Jang, E.W. Shin, J.K. Park, S.I. Choi, Environ. Sci. Technol. 37 (2003) 5062–5070.